



Ignition of hydrogen–air mixtures using pulsed nanosecond dielectric barrier plasma discharges in plane-to-plane geometry



Sharath Nagaraja^{a,*}, Vigor Yang^a, Zhiyao Yin^b, Igor Adamovich^b

^a School of Aerospace Engineering, Georgia Institute of Technology, Atlanta, GA 30332, United States

^b Department of Mechanical and Aerospace Engineering, Ohio State University, Columbus, OH 43210, United States

ARTICLE INFO

Article history:

Received 4 June 2013

Received in revised form 22 August 2013

Accepted 5 October 2013

Available online 22 October 2013

Keywords:

Plasma assisted combustion

Laser Induced Fluorescence

Nanosecond plasma discharge

Plasma fluid modeling

ABSTRACT

Ignition of preheated (400–500 K) H₂–air mixtures at low pressures (80–100 torr) excited by pulsed nanosecond dielectric barrier discharges is investigated through experiments and simulations. Time resolved absolute OH concentration and temperature data are obtained using Laser Induced Fluorescence (LIF) technique. Ignition is achieved in the decaying plasma after a burst of discharge pulses (repetition rate 10–40 kHz), with the time delay inferred from sudden rise in OH⁺ emission. One-dimensional simulations are performed to obtain information about the plasma generated radicals and heat release across the discharge gap. A plasma fluid formulation is used with ions and neutral species at gas temperature, and electrons in non-equilibrium. An accurate reduced chemistry mechanism is developed through sensitivity analysis to expedite the plasma simulations. The model predictions show excellent agreement with experimental measurements, validating the numerical framework and chemistry data. The input pulse energy and ignition characteristics are found to be highly sensitive to uncertainties in dielectric properties. Ignition delay exhibits a threshold-like dependence on input plasma energy, and increases steeply as the number of pulses in the burst is reduced. The nanosecond plasma assisted ignition is achieved through a two-step process. Firstly, the burst of discharge pulses produce a large pool of radicals and provide an average temperature rise of ~1–2 K/pulse. In the next step, if the temperature exceeds a threshold value of ~700 K, significant heat release from partial fuel oxidation is triggered. The process becomes self-sustaining and the temperature continues to rise even after the plasma source is switched off, accelerating the conventional H₂–O₂ chain branching pathways and leading to ignition. We provide conclusive evidence of large volume ignition with nanosecond plasma as opposed to thermal ignition at a hot-spot. Ignition is first observed at the center of the discharge gap, but the kernel expands rapidly to the entire volume, except near walls where heat losses keep the temperature low. It is demonstrated that the ignition occurs independently at different locations due to local plasma chemistry effects and heat transport does not play a significant role.

© 2013 The Combustion Institute. Published by Elsevier Inc. All rights reserved.

1. Introduction

Non-equilibrium plasma discharges (NPD) have shown great promise in thermal and kinetic enhancement of ignition and combustion at a wide range of pressures, flow velocities and equivalence ratios [1–3]. Experiments have demonstrated successful ignition and flame stabilization with plasma assistance at the low pressures and small flow residence times encountered in high-speed propulsion systems [4–6], as well as at the high pressures (1 to several bars) relevant to gas turbine and IC engine applications [7–9]. A variety of NPD systems such as pulsed coronas [10], microwave discharges [11], magnetic gliding arcs [12], and pulsed nanosecond volume discharges [1–4] have been studied

for potential combustion applications. High-voltage, nanosecond duration pulses applied at kHz repetition rates create volumetric plasma with E/N (ratio of electric field magnitude to number density) in the range of 100–1000 Td (1 Td = 10^{–17} V cm²) [3]. The discharge develops in the form of fast ionization waves with a large fraction of input energy consumed in molecular dissociation and excitation of internal energy modes. The pulse duration (10–100 ns), is much shorter than the characteristic timescales for development of ionization instabilities. These features allow nanosecond discharges to generate a large number of active radical species at much higher pressures and power loadings, and lower power budgets as compared to other plasma discharge systems [3].

The nanosecond plasma can be a source of heat and reactive chemical species. Starikovskii and co-workers [13–15] performed shock tube experiments in which a fuel–air mixture was preheated by a shock wave above the ignition temperature. Radicals

* Corresponding author.

E-mail address: sharath@gatech.edu (S. Nagaraja).

generated by a single nanosecond pulse discharge triggered chain branching processes leading to reduction in ignition delay by 1–2 orders of magnitude for a variety of fuels. The additional heating produced by the discharge pulse played only a minor role.

Over the past few years, the flow reactor experiments described in Refs. [16–20] have focused on understanding ignition of fuel–air mixtures excited by pulsed nanosecond plane-to-plane dielectric barrier discharges (NS DBDs) under mildly preheated conditions (100–200 °C). Intensified charge coupled device (ICCD) images demonstrate that pulsed NSDBDs are uniform and devoid of any filaments in air [16] and preheated H₂–air [17–20] in 40–100 torr pressure range. Discharge uniformity is necessary, if non-equilibrium chemistry is to be separated from thermal effects occurring in filaments and hot-spots. In addition, a diffuse volume filling plasma facilitates optical diagnostics and experimental reproducibility. In this configuration, ignition delay [17] and OH concentration [18] were measured in mildly preheated (100–200 °C) H₂–air mixtures subjected to nanosecond voltage waveforms. The number of pulses leading to ignition was found to be a weak function of mixture equivalence ratio, but showed a non-linear dependence on pulsing frequency. At a given temperature and pressure, there existed an optimum repetition rate at which the number of pulses needed for ignition reached a minimum. Reduction in coupled pulsed energy at high repetition rates, due to increase in residual electron density, has been suggested as a possible cause for this behavior. Recent pulse energy measurements in air [16] did not show significant reduction in coupled energy at high repetition rates, suggesting a more comprehensive kinetic analysis is necessary to explain this phenomenon.

In Yin et al. [17,18], sustained application of voltage pulses at a high repetition rate “masked” the sensitivity of ignition characteristics to the details of plasma kinetics. In order to circumvent this behavior, experiments were recently conducted in a decaying plasma after a burst of discharge pulses [19,20]. The ignition characteristics were found to be highly sensitive to temperature and radical concentration at the end of a pulse burst. Ignition delay increased steeply as the number of pulses in the discharge burst was reduced. Kinetic model calculations showed that rise in temperature and H atom concentration beyond a critical threshold triggered chain reaction pathways leading to ignition. The combination of thermal and kinetic effects resulted in a reduction of threshold ignition temperature by ~200 K as compared to thermal ignition. It should be noted that the species and temperature measurements in the plasma flow reactor experiments were conducted in the central region of the discharge volume. The heating and species production rates near the plasma boundary (sheath) layers, however, are uncertain.

High-fidelity numerical models coupled with detailed chemistry mechanisms can complement experiments in study of thermal and non-thermal aspects of plasma assisted ignition and combustion. The wide disparity in timescales offer enormous computational challenges, and it is difficult to resolve important physical phenomena without compromising the accuracy of the results. A self-consistent multi-scale numerical framework for studying the spatio-temporal evolution of nanosecond plasma over multiple voltage pulses was established in [21]. One-dimensional simulations of pulsed NS DBDs in air were conducted in a plane-to-plane geometry in the pressure and pulsing frequency range of 40–100 torr and 1–10⁵ Hz respectively. The model predictions were validated against experimental measurements [16] and results from a quasi-1D analytical model [22] of nanosecond discharges. The input electrical energy remained fairly constant on a per molecule basis from pulse to pulse. Repetitive pulsing generated atomic oxygen in the discharge volume via electron impact dissociation during voltage pulses, and through quenching of excited nitrogen molecules in the afterglow. Ion Joule heating during each voltage

pulse caused a rapid rise of temperature (30–40 K) in the cathode sheath layers. Wall heat loss in the time interval between discharge pulses, however, prevented overheating near the boundaries. The volumetric heat release from quenching of excited species resulted in a “hat shaped” temperature profile after multiple discharge pulses.

In the present work, we perform comprehensive experimental and numerical investigations of pulsed nanosecond plasma assisted H₂–air (mildly preheated) ignition in a plane-to-plane geometry. Time resolved OH concentration and temperature are obtained from LIF measurements in the center of the discharge volume. Ignition is achieved in the decaying plasma after a burst of discharge pulses. One-dimensional simulations are performed to obtain information of the plasma generated radicals and heat release across the discharge gap. The uniform and diffuse nature of the preheated H₂–air plasma [16–20] justifies the 1D assumption. The accuracy of the model is assessed by comparing against OH concentration, temperature and ignition delay measurements after a burst of discharge pulses [19,20]. An accurate reduced chemistry mechanism is developed through sensitivity analysis to expedite the plasma ignition simulations. The sensitivity of input pulse energy and ignition characteristics to residual electron density and dielectric properties is analyzed. Electric field transients during each nanosecond pulse, and spatial evolution of gas temperature, excited species and radicals until ignition (ms timescales) are studied in detail. A special focus of this work is the question whether nanosecond pulsed plasma can produce volumetric ignition. The growth rate of the ignition kernel is studied in detail, investigating the roles played by heat transport and local radical chemistry.

2. Experimental setup

A schematic of the experimental setup used in the present work is shown in Fig. 1. It is similar to the one used in previous studies and described in detail in [18–20]. Briefly, a rectangular cross-section quartz channel (280 mm length, 22 mm breadth, 10 mm height, wall thickness 1.75 mm) is used as the discharge cell. Two plane quartz windows are fused to the ends of the channel, providing optical access in the axial direction. The entire assembly is heated in a tube furnace to improve plasma stability. The fuel and air flows are premixed before the cell inlet. The flow rates through the reactor are controlled by mass flow controllers. Two rectangular copper plate electrodes (14 mm width and 60 mm length) are placed on the top and bottom of the quartz channel. In order to reduce air gaps and prevent corona discharge outside the discharge cell, a 1/16 inch. thick high-temperature dielectric sheet (perfluoroelastomer – Kalrez, DuPont) is placed between each electrode and the channel wall.

The electrodes are connected either to a Chemical Physics Technologies (CPT) or to an FID GmbH high voltage pulsed power supply. The CPT pulser is capable of producing 25 kV peak voltage, 25 ns duration pulses at repetition rates up to 50 kHz. The FID pulser can produce 30 kV, 5 ns pulses up to 100 kHz repetition rates. When CPT pulser is connected to the electrodes, the discharge cell is irradiated by a UV emission source (Hg–Ar lamp) to produce breakdown by the first discharge pulse. No pre-ionization is necessary when FID pulser is in operation. Ignition is detected by monitoring OH* emission through the cell side wall with the help of a narrow bandpass filter (centered at 310 ± 2 nm, bandpass 10 ± 2 nm FWHM), a photomultiplier (PMT) and a digital oscilloscope.

The OH LIF apparatus is similar to one used in [18] and consists of a Nd:YAG laser (532 nm second harmonic output) pumping a tunable dye laser generating output near 615 nm, which is then frequency doubled using a BBO crystal. The laser beam is softly

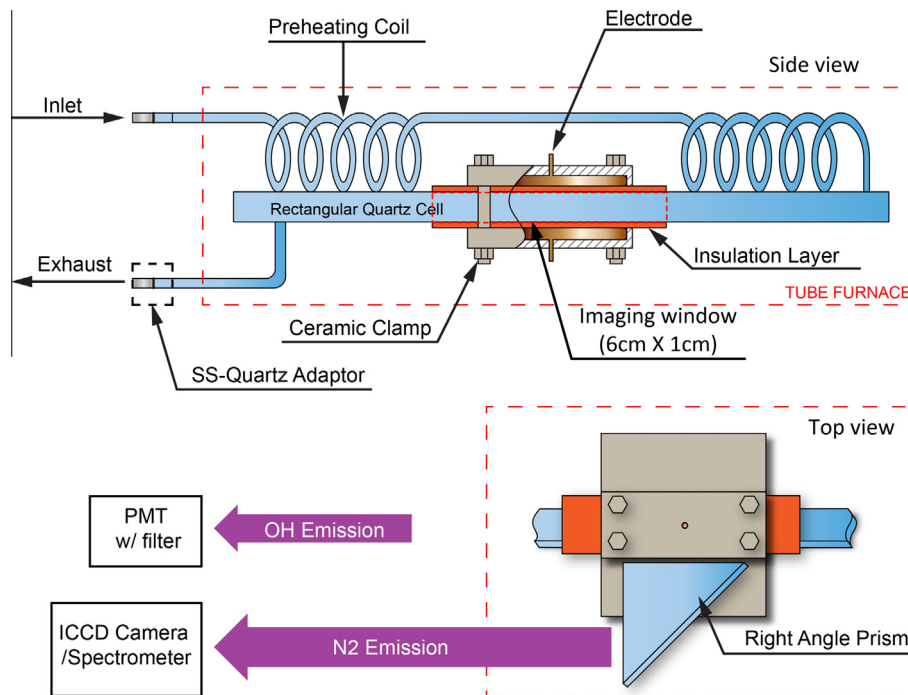


Fig. 1. Schematic of high temperature discharge cell used for plasma assisted ignition experiments.

focused using a 1000-mm focal-length lens and is aligned along the centerline of the discharge cell. LIF signal from a 3-mm-long region (along the laser beam with an estimated beam waist of 1 mm) located at the geometric center of the discharge volume, is collected 90° to the laser direction via a 60-mm right-angle prism (large enough to cover the entire discharge volume). The signal is collimated and refocused by two fused silica lenses into a detector incorporating an aperture (controlling the collection volume), a UG11 glass filter, and a photomultiplier (PMT)). For LIF operation in the linear regime (below 5 $\mu\text{J}/\text{pulse}$), the UV beam energy is controlled by a pair of half wave plate and a thin film polarizer. PMT saturation is avoided by using a neutral density filter at high signal incidences. The entire LIF signal pulse is integrated and analyzed in real time using a programmable digital oscilloscope with 1 GHz bandwidth. The laser beam is tuned across $R_1(4)$ in the OH A–X (0,0) band. The obtained excitation spectrum is integrated over a wide spectral range to eliminate the dependence on laser line-width, as discussed in Ref. [18]. Temperature necessary for calculating the Boltzmann factor has been measured using LIF thermometry incorporating five transitions in the (1,0) band of the OH A–X system [18]. OH signal is calibrated vs. Rayleigh scattering signal obtained at laser wavelength of 308 nm from the same discharge cell. The procedure of Rayleigh calibration is detailed in [18]. The primary advantage of Rayleigh calibration over the traditional Hencken adiabatic burner calibration approach [20] is that it enables *in situ* calibration using the same optical/signal collection system. This is critical for accurate determination of the optical collection efficiency inferred from the calibration process. The total uncertainty in the measured absolute OH number density is estimated to be $\pm 20\%$.

3. Theoretical framework

In the present work, we extend the numerical model described in [21] to simulate ignition of preheated H_2 –air mixtures excited by pulsed NS DBD. The electron transport and reaction coefficients are expressed as functions of electron energy using BOLSIG [23]

and updated at every time-step through interpolation. The transport of species and energy is approximated using the drift-diffusion model. Equations for electric potential, electron energy, and charged and neutral species continuity are considered. In addition, the conservation equations for mass, momentum and energy of the gas mixture are solved simultaneously to model flow motions.

3.1. Model configuration

Figure 2a shows a schematic of the physical configuration with the 1D simulation domain marked using a dashed line. The model calculations are performed at a particular cross-section of the plasma flow reactor setup shown in Fig. 1. The total distance between the two copper electrodes is ~ 1.7 cm, with the discharge gap (distance between the quartz walls) being 1 cm. The quartz walls are 1.75 mm thick, and separated from each electrode by a 1.58 mm thick high temperature dielectric sheet (Kalrez, Dupont). The discharge gap is filled with a mixture of H_2 and dry air (79% N_2 , 21% O_2). The dielectric constant specified by the manufacturer for Kalrez is $\epsilon_s = 4.9$ [24]. Note that this value of ϵ_s was measured at 1 kHz field frequency, which is much lower than the characteristic frequency used in the present work ($1/(\text{pulse duration}) \sim 10^7$ – 10^8 Hz, see Fig. 2b). In Section 4.2 the dielectric constant of Kalrez is varied between 5 and 9 to understand the sensitivity of input pulse energy and the ignition characteristics on uncertainty in dielectric properties. The dielectric constant of quartz is set at $\epsilon_g = 3.8$ for all simulations in this work. The right electrode is connected to a high voltage power supply (CPT or FID pulser), whereas the left electrode is grounded. The measured nanosecond waveforms are shown in Fig. 2b along with the curve-fits used in present simulations. The CPT waveform consists of a bipolar pulse of duration 50 ns beginning to end, with peak voltages of -22.5 kV and 17.5 kV in the negative and positive half cycles respectively. The incident FID waveform is 10 ns long, followed by two reflected pulses, and is approximated by three Gaussian waves of peak voltages 27.5 kV, -20 kV and 13.5 kV respectively (see Fig. 2b).

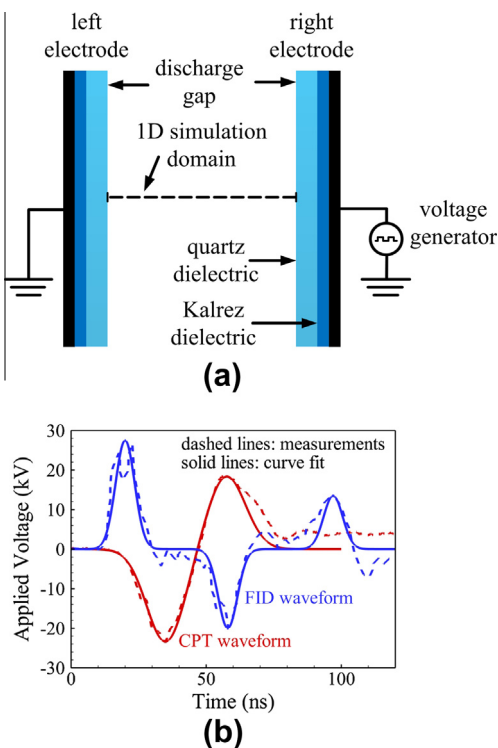


Fig. 2. (a) Schematic of simulation configuration. (b) Experimental waveforms and corresponding curve-fits used in model calculations.

3.2. Numerical methods, initial and boundary conditions

A 2nd order Strang type splitting method is used to treat convection–diffusion and chemical source terms separately [21]. An adaptive time-step approach is utilized to tackle the large disparity in timescales of various physical phenomena of interest. During each discharge pulse, the time-step is varied between 10^{-13} s and 10^{-12} s to accurately capture the electric field transients and the electron energy relaxation process. In the time interval between pulses, the electric field is set to zero and the time-step is fixed at 10^{-9} s. Implicit time integration is performed for stiff chemical source terms, whereas species and flow transport are treated explicitly for computational efficiency. A domain decomposition approach with MPI (message passing interface) is implemented to compute the solution in parallel over multiple processors. Figure 3 shows a grid convergence study for 400, 600, 800 and 1000 node points. The simulations were conducted with an initial pressure of 80 torr and temperature of 473 K. The pulsing rate of the CPT pulser was 60 kHz. In each case, a non-uniform mesh is used with highest resolution near the two dielectric boundaries. Evolution of electron and O atom densities at the center of discharge volume are shown in Fig. 3a. The simulation results with 600, 800 and 1000 grid points are within 1% of each other. The calculations with 400 grid points show ~10% deviation. A similar trend is observed in Fig. 3b which compares the temperature distribution for the four cases. Grid convergence is observed when 600 or more grid points are used in the simulation. In all the following simulations, non-uniform mesh with 600 nodes is used to obtain grid independent solutions.

At solid walls, zero flux boundary condition is imposed for conservation equations of neutral species, mass and momentum. Ion fluxes at the boundaries are expressed as the sum of drift (due to electric field) and thermal velocity components, with the electron flux including a secondary emission component as well. Accurate physical boundary conditions for the gas energy equation are

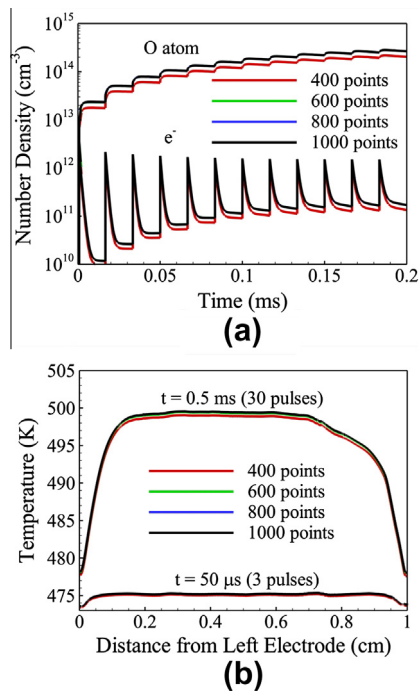


Fig. 3. Comparison between simulation results using 400, 600, 800 and 1000 grid points respectively. (a) Temporal evolution of electron and O atom density at center of discharge volume. (b) Spatial profiles of temperature at the end of 3rd pulse (0.05 ms) and at the end of 30th pulse (0.5 ms) (84 torr, 473 K, 60 kHz, CPT pulser, $\epsilon_s = 9$).

essential to correctly predict the temperature evolution in the discharge volume. Because of low thermal diffusivity of quartz ($1.4 \times 10^{-6} \text{ m}^2 \text{ s}^{-1}$), only a thin portion of the glass layer can be assumed to be affected by the heat transfer from the gas. In this work, we make use of the wall boundary conditions derived in [21] by treating the dielectric layer as a semi-infinite solid. Although we did not restrict the temperature at the wall, it behaves like an isothermal boundary for the timescales of interest. There are no experiments we are aware of which have measured the temperature at the boundary for the present (or similar) configuration. We have, however, compared the model predictions with temperature measurements at the center of discharge volume in air with good agreement [21]. In Section 4, OH concentration and ignition delay measurements at the center of the discharge volume are shown to correlate well with model calculations providing indirect evidence that temperature profiles are correctly predicted in the present simulations. Information about the initial pressure, temperature and equivalence ratio are used to set the initial number densities of $\text{H}_2/\text{O}_2/\text{N}_2$. The remaining species densities are initialized to 10^8 cm^{-3} except for electron density which is initially fixed at $2 \times 10^8 \text{ cm}^{-3}$ to ensure charge neutrality. It has been shown in [21] that initial electron density has no significant effect on plasma properties after breakdown. Owing to pulsed nature of the discharge process considered in this work, photoionization is not important and residual electrons from each pulse provide seed electrons for initiation of the subsequent pulse.

3.3. H_2 -air plasma ignition chemistry

Nanosecond discharges can produce a variety of ions, excited species and radicals. In order to gain quantitative insight into plasma ignition kinetics, a comprehensive chemistry dataset including all the important pathways is necessary. A detailed mechanism consisting of 35 species and 248 reactions was compiled by

combining plasma air chemistry data with conventional H_2 - O_2 reaction kinetics and hydrogen plasma reactions [25,26]. Nitrogen vibrational temperature measured in preheated air (500 K, 100 torr) is quite low, 850 K after 50 pulses and 1050 K after 100 pulses [18]. The reason for this behavior can be attributed to the slow rate of plasma energy addition (0.8–1.0 mJ/pulse) and fast vibrational relaxation. In the present work, since the operating conditions are similar to those in [18], vibrational kinetics are not important, and those processes are not considered as part of the chemistry mechanism (i.e. instantaneous relaxation assumed).

In the present work, our interest is in understanding the low temperature (500–1000 K) plasma chemistry leading to ignition. Under present conditions, the rate coefficient of the chain reaction, $OH + O \rightarrow H + O_2$ critically affects the accuracy of the model predictions. Recent measurements [18,27] suggest that the value given in Popov [26] may not be accurate at low temperatures and is modified in the present work to give $k = 5.3 \times 10^{-11} \text{ cm}^3/\text{s}$ at 500 K. The change is made to ensure the ratio of the forward reaction ($OH + O \rightarrow H + O_2$) and the backward reaction ($H + O_2 \rightarrow O + OH$) rates matches closely ($\pm 50\%$) with the theoretical equilibrium constant value at lower temperatures (below 1000 K). It should be noted that this modification results in over-prediction of $H + O_2 \rightarrow O + OH$ reaction rate constant at higher temperatures (1100–3370 K) compared to the measurements reported in Hong et al. [28], but is well justified for the present low temperature ignition study. In subsequent sections, the simulation results are compared with experimental measurements of the OH concentration, temperature and ignition delay times, to validate the modification made to the $O + OH$ rate constant.

The multi timescale nature of nanosecond pulsed plasma puts enormous burden on simulation time. During each voltage pulse the fast electric field transients following breakdown limit the time-step to be between 10^{-13} and 10^{-12} s. Each voltage pulse requires $\sim 10^5$ time-steps (CPT and FID pulse durations are 100 ns and 120 ns respectively). Computations using the detailed mechanism (compiled from [25,26]) require a prohibitively long time to simulate the entire discharge burst (consisting of 100–130 voltage pulses) and the ensuing ignition process. A sensitivity analysis revealed that nearly half of the species in the detailed mechanism are formed in negligible quantities and do not affect the ignition process. A reduced chemistry dataset consisting of 19 species and 111 reactions has thus been derived for computational efficiency and to perform parametric studies. It incorporates the neutral species N_2 , H_2 , O_2 , H , O , O_3 , OH , HO_2 , and H_2O ; charged species N_2^+ , HN_2^+ , H_3O^+ , O_2^+ , and e^- ; and excited species $N_2(A^3)$, $N_2(B^3)$, $N_2(C^3)$, $N_2(a^1)$ and $O(^1D)$. The details of the chemistry scheme are shown in Appendix 1.

Figure 4 compares the simulation results obtained using reduced and full chemistry schemes with the same operating conditions. A stoichiometric H_2 -air mixture is excited by a burst of 7 ns pulses (CPT waveform) with an initial pressure and temperature of 94 torr and 473 K respectively. Figure 4a shows the evolution of charged species (H_3O^+ , O_2^- and e^-) density at the center of the discharge volume. Calculations with the reduced chemistry scheme fall within 5–10% of those using the detailed scheme. Although not apparent in Fig. 4a, the peak electron density during each voltage pulse is over-predicted by $\sim 5\%$ by the reduced chemistry scheme. N_2^+ ions are produced via electron impact ionization during the breakdown process, but rapidly (in a few ns) reacts with H_2 to form HN_2^+ [26] which is then converted to H_3O^+ through reaction with water molecules [29]. After 5 pulses, H_3O^+ and O_2^- are the major positive and negatively charged species in the system. The decay of electron density after each pulse primarily occurs via recombination with positive ions (HN_2^+ and H_3O^+), and through attachment reaction with O_2 to form O_2^- [26]. Note that under present conditions, because of low ionization fraction

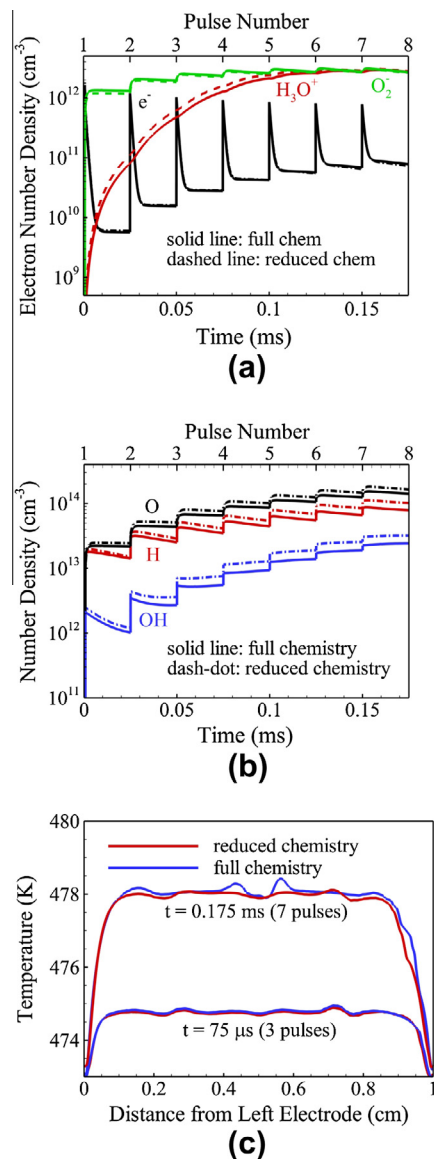


Fig. 4. Comparison between predictions with reduced and full chemistry datasets for a 7 pulse burst. (a) Electron density, (b) neutral species densities, and (c) temperature profile in the domain after 3 and 7 pulses respectively. (94 torr, 473 K, 40 kHz, CPT pulser, $e_s = 9$).

$\sim 10^{-6}$, ion-molecule reactions do not play a significant role in neutral species kinetics. An order of magnitude comparison suggests that the ionization fraction has to increase to $\sim 10^{-4}$ before ion-molecule chemistry becomes important.

Figure 4b shows the evolution of O, H and OH densities at the center of discharge domain. During each voltage pulse, atomic oxygen and hydrogen atoms are produced via electron impact dissociation and quenching of excited N_2 molecules [30,31]. OH is produced from quenching of $O(^1D)$ by H_2 at about 100 ns after each pulse, and from HO_2 over longer timescales [26]. The reduced chemistry mechanism over-predicts the radical concentrations by $\sim 10\%$ compared to the results from the detailed mechanism. The reason for this behavior may be attributed to over-prediction of the peak electron density by the reduced mechanism during each pulse, and the absence of minor channels of electron energy transfer such as formation of $O_2(a^1, b^1)$, dissociation of N_2 . In Fig. 4b, at the end of 7 pulses, the species densities predicted by the reduced scheme remain within 10% of the values obtained from the detailed

mechanism. It must be emphasized that the errors associated with the reduced chemistry scheme do not increase with the number of pulses in the burst.

The performance of the reduced kinetics mechanism is further analyzed by comparing the distribution of temperature in Fig. 4c after 3 and 7 V pulses. At both times, the temperature profiles obtained using the reduced chemistry scheme fall within 1% of the values predicted with the detailed chemistry scheme. It should be noted that the detailed mechanism included a set of NO_x formation and decay reactions taken from Ref. [25]. The sensitivity analysis revealed the concentration of NO produced by the discharge burst is too low to have a significant effect on the evolution of OH density. Hence, we have not considered NO_x kinetics in the reduced chemistry scheme used in the present simulations. In the next section, the simulation results with the reduced chemistry mechanism are validated with experimental measurements of the OH concentration, temperature and ignition delay times, to ensure that all major chemical pathways to describe fuel oxidation are properly considered in the model.

4. Results and discussion

4.1. Electrical characteristics of H₂–air plasma

The applied voltage, gap voltage and conduction current over the duration of a nanosecond discharge pulse (CPT waveform) are shown in Fig. 5a. The simulation is conducted for a stoichiometric H₂–air mixture at 114 torr and 473 K initial pressure and temperature ($\epsilon_g = 3.8$, $\epsilon_s = 9$). Breakdown in the gas volume is observed at ~ 9.5 kV, after which the conduction current rises rapidly to ~ 13 A. Charge accumulation on the dielectric layers creates a strong shielding effect, resulting in the gap voltage and current dropping to near zero within a few ns after breakdown. The current

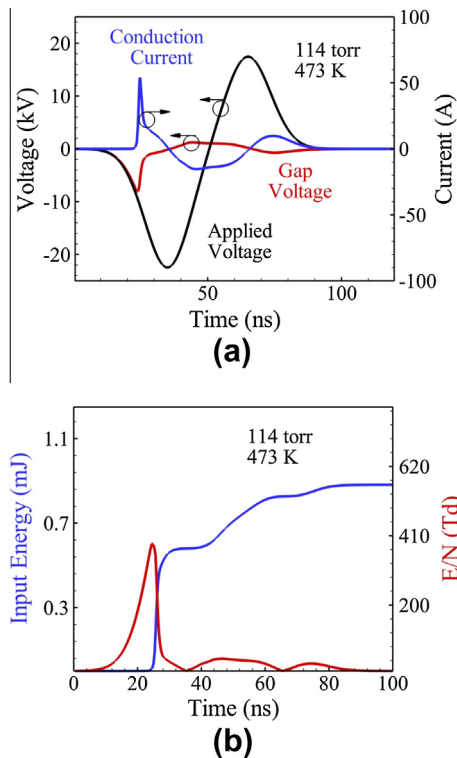


Fig. 5. (a) Voltage current characteristics, and (b) input energy and E/N at center of discharge volume for a single nanosecond pulse in a stoichiometric H₂–air mixture (114 torr, 473 K, CPT pulser, $\epsilon_g = 3.8$, $\epsilon_s = 9$).

changes direction at ~ 36 ns, when the applied voltage begins to drop from its negative peak value. The reduced electric field (E/N) at the center of the discharge gap, and coupled pulse energy are shown in Fig. 5b. About 60% of the total input energy (1 mJ) is coupled during the primary breakdown phase, when peak E/N ~ 400 Td. Note that additional energy coupled when the current reversal occurs goes primarily in vibrational excitation of N₂ molecules (E/N less than 100 Td). CARS measurements of nitrogen vibrational temperature in air [19] under present conditions, however, demonstrates that the vibrational non-equilibrium is insignificant and unlikely to affect the plasma kinetics. In all the modeling results presented in this work, we assume vibrational relaxation to be instantaneous. Figure 6 shows variation in coupled discharge pulse energy for different pulse repetition rates at 114 torr and 473 K initial pressure and temperature. It is evident that the coupled energy changes by less than 10% when the pulsing frequency is increased from 10 to 60 kHz. It appears that the residual electron density, which is a strong function of the pulsing rate, has only a minor effect on input energy.

4.2. Uncertainty in dielectric properties

The effect of uncertainty in dielectric properties on input pulse energy and plasma species production is shown in Fig. 7. A burst of 100 discharge pulses (CPT pulser) at 40 kHz repetition rate is simulated at 80 torr and 473 K initial pressure and temperature. Four cases are considered, with the dielectric constant of Kalrez layer set to $\epsilon_s = 5, 6, 7$ and 9 respectively ($\epsilon_g = 3.8$ for quartz). The input energy per pulse rises by more than 40% as ϵ_s is increased from 5 to 9 as seen in Fig. 7a. An analytical expression for input energy in nanosecond dielectric barrier discharges [22] given below provides insight into this behavior,

$$Q_{pulse} \approx \frac{1}{2} C \left[V_b^2 + V_{peak}^2 \frac{\sqrt{2\pi}}{\tau/RC} \right] \quad (1)$$

where V_b and V_{peak} are breakdown voltage and peak voltage respectively, R the resistance of shielded plasma after breakdown, and τ the pulse duration parameter in the Gaussian fit of voltage waveform. C is the effective capacitance of dielectric layers obtained from the following equation:

$$C = \epsilon_0 A \left[\frac{\epsilon_s}{2l_s} + \frac{\epsilon_g}{2l_g} \right] \quad (2)$$

where l_g and l_s are the thickness of quartz and Kalrez layers respectively, and A the electrode surface area. It is evident that increase in dielectric constants or decrease in thickness of the two layers has the effect of increasing the capacitance and hence the coupled pulse energy. Figure 7b shows variation in atomic oxygen density and temperature at center of discharge volume for different dielectric constants for Kalrez layer. For $\epsilon_s = 5$, the temperature at the end

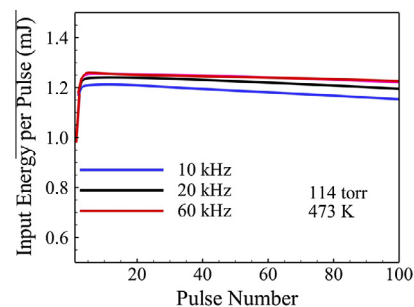


Fig. 6. Input energy per pulse as a function of repetition rate for a burst of 100 pulses (114 torr, 473 K, CPT pulser, $\epsilon_g = 3.8$, $\epsilon_s = 9$).

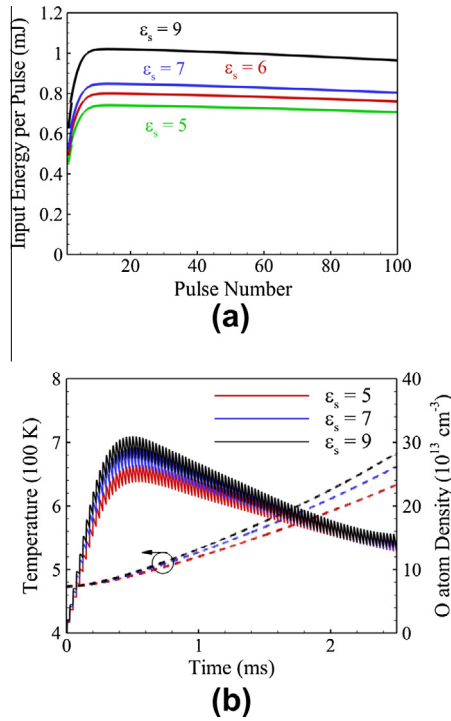


Fig. 7. Variation in (a) input pulse energy, and (b) O atom density and temperature at center of discharge volume for different dielectric constant values of Kalrez layer (80 torr, 473 K, 40 kHz, CPT pulser, $\epsilon_g = 3.8$).

of the burst is 625 K, whereas for $\epsilon_s = 9$, it is $\sim 10\%$ higher at 680 K. As discussed in Section 4.3, the $\text{H}_2\text{-O}_2$ chain branching pathways “take-off” above a threshold temperature of ~ 700 K. As a consequence, the ignition delay time may drop by an order of magnitude when ϵ_s is increased from 5 to 9. Peak O atom density during the burst increases from $2.5 \times 10^{14} \text{ cm}^{-3}$ ($\epsilon_s = 5$) to $3 \times 10^{14} \text{ cm}^{-3}$ ($\epsilon_s = 9$), which is primarily due to increase in rates of electron impact excitation and dissociation (input energy increases with increase in ϵ_s). After 0.5 ms (20 pulses), O atom consumption rate (via formation of OH) exceeds the production rate, irrespective of the ϵ_s value. Consequently, O atom concentration at the end of the burst is not sensitive to changes in the dielectric constant.

4.3. LIF measurements and comparison with model predictions

OH concentration and rotational temperature (assumed to be in equilibrium with the translational temperature) are measured on the centerline of the discharge channel. FID pulser is used for the LIF measurements since it provides a higher input energy per pulse (1.5–2.5 mJ) as compared to the CPT pulser (0.75–1.25 mJ) [17]. Figure 8a shows the comparison between the measured absolute OH concentration and the model predictions after a 50 pulse burst (10 kHz repetition rate) at 100 torr and 500 K initial pressure and temperature ($\epsilon_g = 3.8$, $\epsilon_s = 9$). $\text{H}_2\text{-air}$ equivalence ratios of 0.06 and 0.12 are considered in this study. Temperatures measured at the end of the discharge burst (2 μs after the last pulse) are also plotted for comparison with those predicted by the model. The model calculations agree well with the experimental data lending confidence in the chemistry dataset used and the numerical framework. The peak OH densities ($3 \times 10^{13} \text{ cm}^{-3}$) are not sensitive to changes in equivalence ratio. In addition, there is no transient rise in OH concentration after the pulser is switched off. Model predictions of O and H atom densities after the pulse burst are shown in Fig. 8b. The timescales of decay of O and H densities are similar to that of OH consumption (1–2 ms) under present conditions. Peak

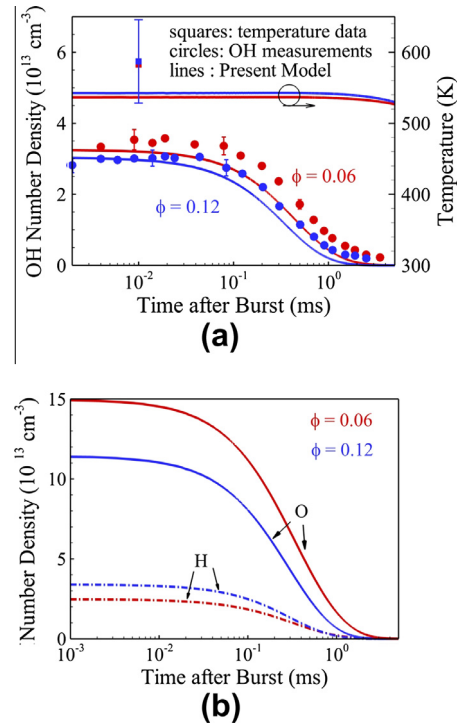


Fig. 8. (a) Comparison between OH and temperature measurements with model predictions, and (b) O and H density decay at center of discharge volume after a 50 pulse burst (100 torr, 500 K, 10 kHz, FID pulser, $\epsilon_g = 3.8$, $\epsilon_s = 6$).

density of H atoms is comparable to OH peak values, but atomic oxygen densities are higher ($1\text{--}1.5 \times 10^{14} \text{ cm}^{-3}$) because of the low equivalence ratios considered ($\phi = 0.06$ and $\phi = 0.12$). Note that O density is quite sensitive to change in equivalence ratio, increasing by nearly 50% when ϕ is decreased from 0.12 to 0.06. The low temperature oxidation process consists of recirculation of H and OH radicals and consumption of O through the following reactions:



The H atom concentration is higher for larger ϕ , which leads to increase in OH and consumption of O via Eqs. (3)–(5). OH is then consumed to produce H via Eq. (6), and the cycle repeats. The net outcome is that O consumption rate increases with ϕ . On the other hand, H and OH balance each other and are weak functions of ϕ .

4.4. Burst mode ignition analysis

A series of experiments and simulations were conducted to investigate ignition of stoichiometric $\text{H}_2\text{-air}$ mixtures in a decaying plasma after a burst of discharge pulses. The model predictions of temperature rise at the center of the discharge volume are shown in Fig. 9a. The initial pressure and temperature are 80 torr and 473 K with $\epsilon_g = 3.8$ and $\epsilon_s = 9$ (CPT pulser, 40 kHz repetition rate). The measurements are made after the end of the discharge burst, with the system allowed to evolve without any further energy addition. A continuous rise in temperature is observed leading to ignition at 1.5 ms after the last discharge pulse for a burst size of 110 pulses. The ignition delay falls to 0.25 ms for a 130 pulse burst,

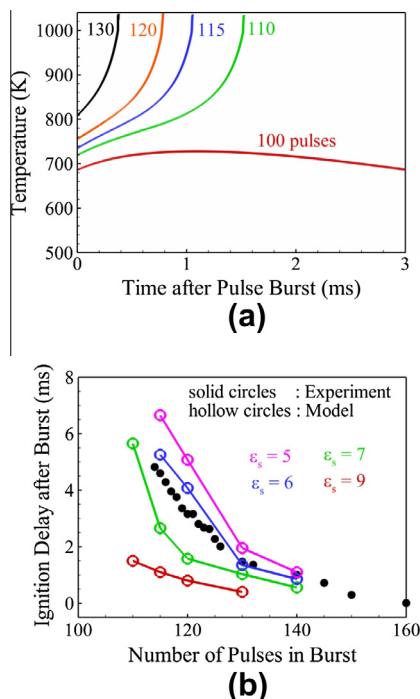


Fig. 9. (a) Temporal evolution of temperature at center of discharge volume for $\epsilon_s = 9$, and (b) ignition delay time as a function of number of voltage pulses in the burst (80 torr, 473 K, 40 kHz, CPT pulser, $\epsilon_g = 3.8$).

demonstrating that the heating and radical pool generated by the nanosecond plasma substantially affect the ignition characteristics. No ignition is observed when the pulse burst is restricted to 100 pulses, with temperature peaking at 710 K (1 ms after the burst), before heat loss from conduction exceeds the chemical heat release in the discharge domain. For a given set of initial conditions, the temperature at the end of the burst is critical to determine whether the mixture ignites or not. In this particular case (Fig. 8), the threshold temperature at the end of pulse burst is ~ 700 K, below which no ignition is observed.

The ignition delay time, shown in Fig. 9b, is calculated for different ϵ_s between 5 and 9, and compared with the experimental data under present conditions. Rapid rise in $OH(A \rightarrow X)$ emission is considered as the indicator of ignition in the experiments. In the simulations, ignition is defined as the point where a sharp “jump” in the temperature profile occurs. The trend in ignition delay reduction with increase in number of pulses in a burst is well reproduced by the model. The figure also illustrates the sensitivity of ignition delay predictions to variation in dielectric properties, with $\epsilon_s = 6$ providing the best match with measurements. This demonstrates that the input energy per pulse is ~ 0.8 mJ (see Fig. 6a) in a stoichiometric H_2 -air plasma under present conditions. The ignition delay times are over-predicted by $\sim 20\%$ if the dielectric constant of Kalrez is taken as 4.9 (manufacturer specifications). This deviation may be because $\epsilon_s = 4.9$ was measured at 1 kHz field frequency, which is much lower than the characteristic frequency used in the present work (inverse of pulse duration $\sim 10^7$ – 10^8 Hz, see Fig. 2b), so ϵ_s may change somewhat at high frequencies. To a small extent, changing the dielectric constant may also be compensating for the inherent uncertainties associated with kinetics and numerical methods used in this work. It must be emphasized that the uncertainty in the dielectric constant does not change the fundamental conclusions of the present work. The ignition delay times exhibit a threshold like dependence on input plasma energy, steeply increasing as number of pulses in the burst is reduced for all the dielectric constant values (5, 6, 7 and 9) considered in the

study. The results confirm a significant effect of plasma chemistry processes on low temperature ignition of H_2 -air mixtures. In summary, Fig. 9b illustrates the importance of using a well characterized dielectric to validate the nanosecond plasma ignition model with measurements.

Figure 10 shows the evolution of dominant radicals and temperature on the discharge centerline after a 120 pulse burst. The other operating conditions are the same as in Fig. 9. The concentrations of O , H , and OH at the end of the pulse burst are approximately 1×10^{14} , 1×10^{15} and 8×10^{13} cm^{-3} , respectively, as seen in Fig. 10a. During the discharge burst, O and H atoms are produced primarily by electron impact dissociation and quenching of excited N_2 molecules during each discharge pulse. OH is produced primarily from quenching of $O(^1D)$ by hydrogen molecules during first few voltage pulses. Reaction of HO_2 with O is the dominant OH production pathway after 0.1 ms (4 pulses). The temperature rise in the discharge volume is ~ 1 K/pulse until 2.5 ms (100 pulses). The quenching of excited species is the primary source of heating in this timescale. Beyond this juncture, a substantial increase in volumetric heating rate is observed owing to fuel oxidation pathways triggered by plasma generated radicals. The dominant chain branching and oxidation processes triggered by radical generation in the plasma are given by following equation:

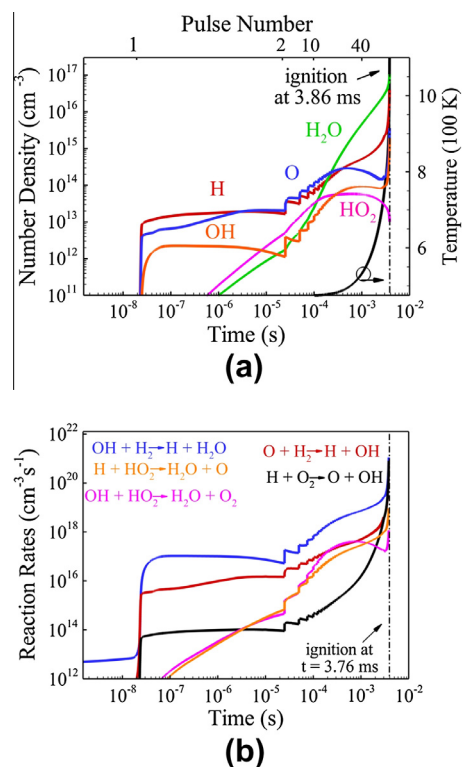
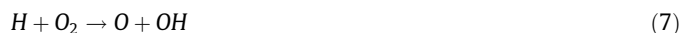


Fig. 10. (a) Evolution of species densities and temperature and (b) dominant chain branching and oxidation reaction rates at center of discharge volume leading to ignition after a burst of 120 pulses (80 torr, 473 K, 40 kHz, CPT pulser, $\epsilon_g = 3.8$, $\epsilon_s = 9$).

The rates of reactions (Eqs. (7)–(11)) at the center of discharge volume are shown in Fig. 10b. Accumulation of atomic oxygen during the discharge burst triggers the chain branching processes of Eqs. (7) and (8). At 1 ms (i.e. after 40 pulses), the increase in reaction rate of Eq. (8) explains the steep reduction in O number density, and rapid rise in H concentration (see Fig. 10a). Note that the chain branching reactions are highly temperature sensitive. The primary oxidation reaction is given by Eq. (10), whereas the other two pathways (Eqs. (10) and (11)) lend minor contributions to H_2O production. Increase in chain branching reaction rates produce OH , which then accelerates the heat release from fuel oxidation. The increase in temperature completes the cycle by further increasing the rates of Eqs. (7) and (8). This non-linear feedback cycle causes an exponential increase in temperature and radical concentration leading to ignition.

It must be emphasized that in the presence of a large pool of radicals generated by a nanosecond discharge burst, heating the gas mixture by exothermic chemical reactions to ~ 700 K is sufficient to achieve ignition after a delay after the burst. Ignition can never be achieved if the nanosecond plasma source is replaced with a uniform heating device which is turned off when the temperature reaches ~ 730 K (heating caused by recombination of all radicals generated during the nanosecond discharge burst can at most result in a temperature rise of about 30 K under present conditions). This suggests that the radicals generated by the plasma initiate oxidation reactions, thereby releasing some of the chemical energy “locked” in the fuel molecules. The temperature rise in Fig. 9a after the end of the pulse burst (after 3 ms) is entirely due to this effect. The rapid heating process continuously accelerates the temperature-sensitive chain branching reactions leading to ignition. A detailed analysis of nanosecond plasma kinetics and ignition was performed by Yin et al. [17]. No ignition was observed in calculations performed by switching off the dominant plasma radical generation processes after a discharge burst (end temperature 700 K). The mixture had to be heated to a centerline temperature of 900 K in order to achieve thermal ignition.

The spatial evolution of temperature, shown in Fig. 11, reveals further interesting features of nanosecond plasma assisted ignition. The operating conditions are the same as in Fig. 9. The model prediction on a relatively short timescale (burst duration less than 0.5 ms) is shown in Fig. 11a. During each discharge pulse, ion Joule heating in the cathode sheath layers results in rapid increase in temperature of ~ 30 K near the walls. A similar behavior was observed for nanosecond discharges in air [21]. Quenching of excited species in the plasma volume results in a steady rise in temperature of ~ 1 – 2 K/pulse throughout the discharge burst. It can be observed that the temperature profiles are not exactly symmetric in Fig. 11a at smaller timescales (less than 1 ms). This is because breakdown in the discharge volume occurs only during the first rise in applied voltage resulting in asymmetry in the time-dependent electric field pulse (such as shown in Fig. 5b) which governs the uniformity of species production and heating rates. If the applied voltage pulses had alternating polarity (positive, negative, positive), and separated by a few tens of microseconds to allow breakdown during every pulse (positive and negative), this would produce a symmetric plasma. Heat and mass transport over longer timescales (>1 ms) tend to even out the non-uniformity and result in symmetric profiles as seen in Fig. 11b. The temperature distribution after 60 pulses is almost flat, with lower values near the boundaries because of heat loss by conduction to the walls. By the end of the discharge burst (after 120 pulses), the peak temperature at the center is ~ 730 K. As discussed earlier, heat release from partial fuel oxidation continues to increase the temperature after the plasma source is turned off. The temperature profile, however, exhibits a more pronounced maximum near the centerline, as seen at 3.75 ms. Ignition is first observed at the center where a

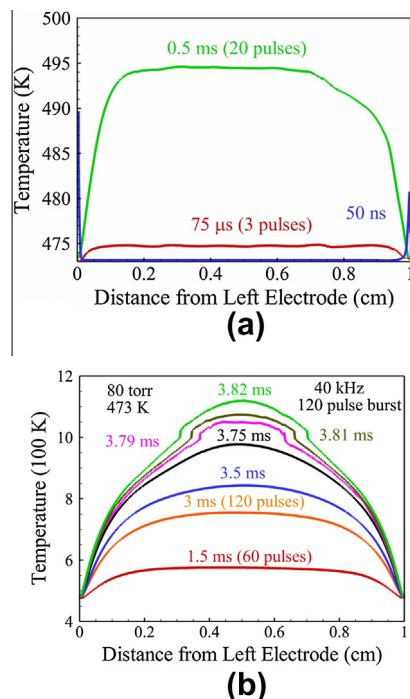


Fig. 11. Spatial distribution of temperature at different times showing the expansion of the ignition kernel after a 120 pulse burst (80 torr, 473 K, 40 kHz, CPT pulser, $\epsilon_g = 3.8$, $\epsilon_s = 9$).

sudden jump in temperature is observed at approximately 3.76 ms. The ignition kernel expands rapidly outwards at a rate of ~ 30 ms^{-1} . For comparison, the unstretched laminar flame speed for a stoichiometric H_2 –air mixture at 0.2 atm has been reported to be ~ 2 ms^{-1} [32]. It must be emphasized that under present conditions, flame (if present) is propagating into a preheated mixture doped with radicals from the discharge burst. Hence, the actual flame speed may be higher than the speed of a laminar flame propagating into an unburnt mixture. Note that the laminar flame speed is used as a reference since it denotes the rate at which heat is transported from burnt to unburnt gases. It does not imply that a deflagration wave is responsible for the growth of the ignition kernel with the nanosecond plasma source. In Fig. 12, the heat and radicals produced by the nanosecond plasma source brings the entire discharge volume to a “self-ignition” threshold, and heat transport alone cannot explain the rate at which ignition kernel expands.

There are two possible mechanisms controlling the growth of the ignition kernel. (a) Local plasma radical chemistry processes can bring the mixture to ignition threshold, after which it ignites after a time delay. (b) Heat transport from the core of the ignition kernel raises the temperature near the boundaries to the ignition threshold, leading to flame propagation into the unburnt mixture. In order to explore the role of heat transport, we performed 0D time accurate simulations at each spatial location using the species concentration, temperature and pressure predicted by the 1D calculations at the end of the discharge burst as initial conditions. The spatial evolution of temperature after the discharge burst as predicted by the 1D model and “local” 0D simulations is shown in Fig. 12. It is clear that the ignition kernel expands at nearly the same rate with or without heat transport. This demonstrates that ignition is achieved in a “lagging” fashion at different locations in the discharge volume, when the radicals and heating produced by the plasma take the mixture above a threshold temperature (~ 700 K under present conditions). Note that the 1D model considers compressibility effects, unlike the 0D calculations. The close match between the two results demonstrates that the compression

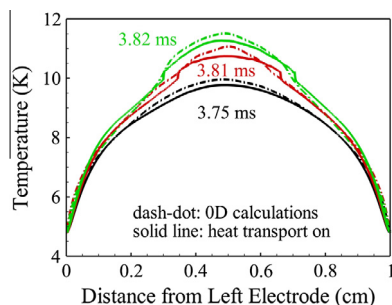


Fig. 12. Spatial distribution of temperature during ignition with and without considering heat transport processes after a 120 pulse burst (80 torr, 473 K, 40 kHz, CPT pulser, $\epsilon_g = 3.8$, $\epsilon_s = 9$).

waves generated during the discharge pulses have practically no impact on the ignition characteristics.

Figure 13 shows a series of ICCD camera images of nanosecond discharge and ignition in a stoichiometric H_2 -air mixture. The initial pressure and temperature are 104 torr and 473 K respectively (CPT pulser, 40 kHz repetition rate). The plasma images were taken during individual discharge pulses, whereas the flame images were taken after the end of the burst. It is clear that the plasma is uniform and diffuse throughout the burst after the first few pulses. The spatial effects observed from the ICCD camera are both in directions parallel and normal to the dielectric. Ignition is first observed at the edge of the electrodes, as shown in Fig. 13 (possibly due to higher electric fields at the corners of the electrodes), but is rapidly followed by ignition at multiple locations along the centerline of the discharge volume. The emission then spreads to occupy the entire volume between the electrodes within 0.2 ms. If attention is focused on a particular cross section, it can be observed that ignition first occurs at the center and spreads rapidly towards the two boundaries. The present one-dimensional simulations of the discharge suggest the same behavior, as elaborated previously.

Figures 14 and 15 show the spatial distribution of dominant chemical species across the discharge gap for ignition in a stoichiometric H_2 -air mixture after a 120 pulse burst. The operating conditions are the same as in Fig. 10. The peak H atom density increases ~ 12 times from $2 \times 10^{15} \text{ cm}^{-3}$ at 3 ms to $25 \times 10^{15} \text{ cm}^{-3}$ after ignition (3.82 ms), as evident in Fig. 14a. The evolution of atomic oxygen is similar, as shown in Fig. 14b. A small increase in temperature near ignition significantly increases the chain branching reaction rates. As a consequence, the radical concentration profiles are much steeper than the temperature distribution, with well pronounced maxima near the centerline.

OH and H_2O distributions are shown in Fig. 15a and b respectively. Peak value of OH concentration increases by ~ 20 times after ignition, from $1 \times 10^{14} \text{ cm}^{-3}$ to $2 \times 10^{15} \text{ cm}^{-3}$. Water concentration increases at a somewhat slower rate, rising by 10 times after ignition, although the absolute values are much higher. It is interesting to notice that both OH and H_2O profiles exhibit secondary peaks near the dielectric boundaries. During the discharge burst,

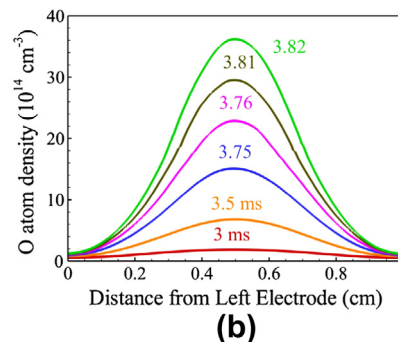
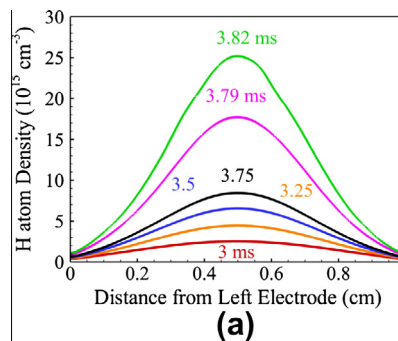


Fig. 14. Spatial distribution of (a) H and (b) O number densities across the discharge gap at different times leading to ignition after a 120 pulse burst (80 torr, 473 K, 40 kHz, CPT pulser, $\epsilon_g = 3.8$, $\epsilon_s = 9$).

higher E/N values near cathode sheath edges result in higher radical production rates compared to the central portion of the plasma volume. In the decaying plasma after the burst, however, electric field effects are completely absent and cannot account for the secondary peaks near the boundaries. A continuous flux of H radicals from the center towards the boundaries aids in the formation of HO_2 via the three body reaction $H + O_2 + M \rightarrow HO_2 + M$. Lower temperatures result in 5–8 times higher HO_2 densities near the boundaries than at the center of the discharge gap (see Fig. 15c). OH production near the boundaries is primarily from the reaction $HO_2 + H \rightarrow OH + OH$. Finally, secondary peaks in H_2O profiles near the walls are due to reactions $OH + HO_2 \rightarrow H_2O + O_2$ and $H + HO_2 \rightarrow H_2O + O$.

5. Conclusions

Experiments and one-dimensional simulations were conducted to provide insight into the ignition of H_2 -air mixtures excited by pulsed nanosecond dielectric barrier discharges. The gas mixture was mildly preheated (400–500 K) to create diffuse and uniform plasma in a parallel plate discharge cell. The studies were performed in a decaying plasma after a burst of high-voltage pulses. The temporal evolution of temperature and OH concentration were

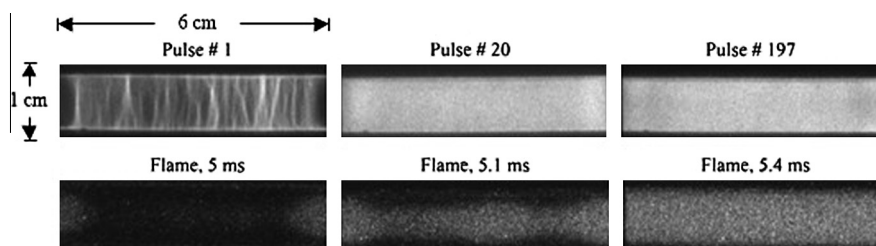


Fig. 13. ICCD images of nanosecond plasma and ignition in a stoichiometric H_2 -air mixture (104 torr, 473 K, 40 kHz, CPT pulser). The camera gate is 2 μs for plasma images and 30 μs for flame images.

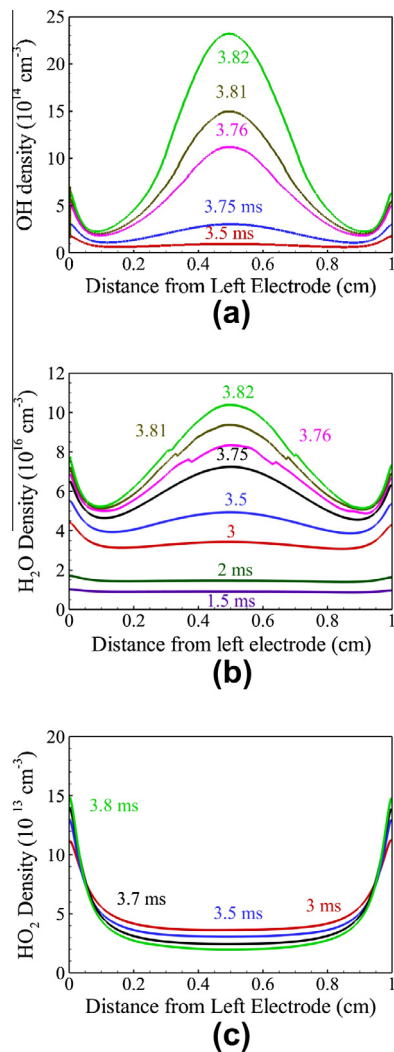


Fig. 15. Spatial distribution of (a) OH, (b) H₂O and (c) HO₂ number densities across the discharge gap at different times leading to ignition after a 120 pulse burst (80 torr, 473 K, 40 kHz, CPT pulser, $\epsilon_g = 3.8$, $\epsilon_s = 9$).

measured at the centerline using the LIF technique. A self-consistent plasma fluid framework was utilized to simulate the species and temperature evolution across the electrode gap over ns–ms timescales. A reduced chemistry mechanism consisting of 19 species and 111 reactions was inferred through sensitivity analysis. The model predictions showed good agreement with OH concentration, temperature and ignition delay measurements. At the present conditions, since the energy was added to the plasma relatively slowly, vibrational non-equilibrium did not play a significant role in plasma kinetics (due to rapid relaxation). However, this may not be the case when energy is added rapidly, such as in a discharge filament.

Both the experiments and simulations showed that the ignition characteristics were highly sensitive to input plasma energy. Changing the dielectric constant of Kalrez from 5 to 9 produced significant variations in ignition delay predictions, with $\epsilon_s = 6$ provided the best match between measurements and calculations. The effectiveness of plasma generated radicals in triggering partial fuel oxidation was found to depend on the temperature at the end of the pulse burst (T_f). When T_f exceeded 700 K, the temperature continued to rise even after the plasma source was switched off. Acceleration of the conventional H₂–O₂ chain branching pathways resulted in ignition after a short time delay after the burst. Both

ICCD camera images and model predictions showed that ignition first occurs along the centerline of the discharge cell. The kernel then spread rapidly towards the boundaries, encompassing the entire volume within 0.2 ms after the first ignition event. The expansion rate of the ignition kernel remained unaltered even when the heat transport processes were switched off (comparing original 1D results with “local” OD calculations). This suggested that the ignition kernel growth is primarily due to local plasma chemistry effects and not due to heat and radical transport from the center towards the boundaries. The nanosecond pulse discharge plasma excitation resulted in nearly simultaneous ignition over a large volume, in sharp contrast to hot-spot igniters. This work demonstrated that the low-temperature plasma-assisted ignition in H₂–air is well understood, i.e. that kinetics incorporated into the model described fuel oxidation by reactions of plasma-generated radicals, resultant temperature rise, and ignition adequately.

Acknowledgments

This work was supported by MURI research grant FA9550-09-0602 from the Air Force Office of Scientific Research, with Dr. Chipping Li as technical monitor.

Appendix A. Supplementary material

Supplementary data associated with this article can be found, in the online version, at <http://dx.doi.org/10.1016/j.combustflame.2013.10.007>.

References

- [1] S.M. Starikovskaia, *J. Phys. D-Appl. Phys.* 39 (16) (2006) R265–R299.
- [2] A. Yu Starikovskii, *Proc. Combust. Inst.* 30 (2) (2005) 2405–2417.
- [3] A. Starikovskiy, N. Aleksandrov, *Prog. Energy Combust. Sci.* 39 (1) (2013) 61–110.
- [4] A. Dutta, Z. Yin, I.V. Adamovich, *Combust. Flame* 158 (8) (2011) 1564–1576.
- [5] S.B. Leonov, D.A. Yarrantsev, A.P. Napartovich, I.V. Kochetov, *Plasma Sci. IEEE Trans.* 34 (6) (2006) 2514–2525.
- [6] S.B. Leonov, D.A. Yarrantsev, A.P. Napartovich, I.V. Kochetov, *Plasma Sci. Technol* 9 (6) (2008) 760.
- [7] C.D. Cathey, T. Tang, T. Shiraishi, T. Urushihara, A. Kuthi, M.A. Gundersen, *Plasma Sci. IEEE Trans.* 35 (6) (2007) 1664–1668.
- [8] K. Criner, A. Cessou, J. Louiche, P. Vervisch, *Combust. flame* 144 (1–2) (2006).
- [9] W. Kim, H. Do, M.G. Mungal, M.A. Cappelli, *IEEE Trans. Plasma Sci.* 34 (6) (2006) 2545–2551.
- [10] F. Wang, J.B. Liu, J. Sinibaldi, C. Brophy, A. Kuthi, C. Jiang, P. Ronney, M.A. Gundersen, *IEEE Trans. Plasma Sci.* 33 (2) (2005) 844–849.
- [11] E.S. Stockman, S.H. Zaidi, R.B. Miles, C.D. Carter, M.D. Ryan, *Combust. Flame* 156 (7) (2009) 1453–1461.
- [12] T. Ombrello, Y. Ju, A. Fridman, *AIAA J.* 46 (10) (2008) 2424–2433.
- [13] I.N. Kosarev, N.L. Aleksandrov, S.V. Kindysheva, S.M. Starikovskaia, A. Yu Starikovskii, *Combust. Flame* 154 (3) (2008) 569–586.
- [14] I.N. Kosarev, N.L. Aleksandrov, S.V. Kindysheva, S.M. Starikovskaia, A. Yu Starikovskii, *J. Phys. D: Appl. Phys.* 41 (3) (2008) 032002.
- [15] I.N. Kosarev, N.L. Aleksandrov, S.V. Kindysheva, S.M. Starikovskaia, A. Yu Starikovskii, *Combust. Flame* 156 (1) (2009) 221–233.
- [16] K. Takashima, Z. Yin, I.V. Adamovich, *Plasma Sour. Sci. Technol.* 22 (1) (2013) 015013.
- [17] Z. Yin, K. Takashima, I.V. Adamovich, *IEEE Trans. Plasma Sci.* 39 (12) (2011) 3269–3282.
- [18] Z. Yin, C.D. Carter, W.R. Lempert, I.V. Adamovich, *Combust. Flame* 160 (9) (2013) 1594–1608.
- [19] I. Choi, Z. Yin, I.V. Adamovich, W.R. Lempert, *IEEE Trans. Plasma Sci.* 39 (12) (2011) 3288–3299.
- [20] Z. Yin, I.V. Adamovich, W.R. Lempert, *Proc. Combust. Inst.* 34 (2013) 3249–3258.
- [21] S. Nagaraja, V. Yang, I.V. Adamovich, *J. Phys. D Appl. Phys.* 46 (15) (2013) 155205.
- [22] I.V. Adamovich, M. Nishihara, I. Choi, M. Uddi, W.R. Lempert, *Phys. Plasmas* 16 (2009) 113505.
- [23] G.J.M. Hagelaar, L.C. Pitchford, *Plasma Sour. Sci. Technol.* 14 (4) (2005) 722.
- [24] <<http://o-ring.info/en/datasheets/kalrez/ERIKS%20-%20Kalrez%203018.pdf>>.
- [25] M. Uddi, N. Jiang, I.V. Adamovich, W.R. Lempert, *J. Phys. D Appl. Phys.* 42 (7) (2009) 075205.
- [26] N.A. Popov, *Plasma Phys. Rep.* 34 (5) (2008) 376–391.
- [27] A.A. Konnov, *Combust. Flame* 152 (4) (2008) 507–528.

- [28] Z. Hong, D.F. Davidson, E.A. Barbour, R.K. Hanson, Proc. Combust. Inst. 33 (2011) 309–316.
- [29] N.L. Aleksandrov, S.V. Kindysheva, M.M. Nudnova, A. Yu Starikovskiy, J. Phys. D Appl. Phys. 43 (25) (2010) 255201.
- [30] G.D. Stancu, F. Kaddouri, D.A. Lacoste, C.O. Laux, J. Phys. D Appl. Phys. 43 (12) (2010) 124002.
- [31] M. Uddi, N. Jiang, E. Mintusov, I.V. Adamovich, W.R. Lempert, Proc. Combust. Inst. 32 (1) (2009) 929–936.
- [32] M. Kuznetsov, S. Kobelt, J. Grune, T. Jordan, Int. J. Hydrogen Energy 37 (22) (2012) 17580–17588.